







UOCS-IX. AstroSat/UVIT Study of the Open Cluster NGC 2818: Blue Stragglers, Yellow Stragglers, Planetary Nebula, and their Membership

Sharmila Rani^{1,2} , Gajendra Pandey¹ , Annapurni Subramaniam¹ , and N. Kameswara Rao¹ ¹ Indian Institute of Astrophysics, Bangalore, 560034, India; sharmila.rani@iiap.res.in² Pondicherry University, R.V. Nagar, Kalapet, 605014, Puducherry, India

Received 2022 November 26; revised 2022 December 27; accepted 2023 January 4; published 2023 March 1

Abstract

We present the first far-UV (FUV) imaging results of the intermediate-age Galactic open cluster NGC 2818 that has a planetary nebula (PN) within the field using images taken from the Ultra Violet Imaging Telescope (UVIT) aboard AstroSat. We identify cluster members by combining UVIT-detected sources with Gaia EDR3 data. We detect four bright and hot blue straggler stars (BSSs) and two yellow straggler stars (YSSs) based on their location in optical and FUV–optical color–magnitude diagrams. Based on the parameters estimated using spectral energy distributions, we infer that BSSs are either collisional products or might have undetectable white dwarf (WD) companions. Our photometric analysis of YSSs confirms their binarity, consistent with the spectroscopic results. We find YSSs to be formed through a mass-transfer scenario and the hot components are likely to be A-type subdwarfs. A comparison of the radial velocity, Gaia EDR3 proper motion of the PN with the cluster, and reddening toward the PN and the cluster does not rule out the membership of the PN. Comparing the central star’s position with theoretical post-AGB (pAGB) models suggest that it has already entered the WD cooling phase, and its mass is deduced to be $\sim 0.66 M_{\odot}$. The corresponding progenitor mass turns out to be $\sim 2.1 M_{\odot}$, comparable to the turn-off mass of the cluster, implying that the progenitor could have formed in the cluster. We suggest that the NGC 2818 might be one of the few known clusters to host a PN, providing a unique opportunity to test stellar evolution models.

Unified Astronomy Thesaurus concepts: Milky Way Galaxy (1054); Open star clusters (1160); Blue straggler stars (168); Yellow straggler stars (1829); Ultraviolet photometry (1740); Ultraviolet observatories (1739); Hertzsprung Russell diagram (725); Planetary nebulae (1249)

1. Introduction

Open clusters (OCs) are ideal laboratories to probe the structure and history of the Galactic disk. They are also testbeds to study the formation and evolution of single and binary stellar populations. Dynamical interactions of stellar populations in star clusters lead to binaries and the formation of exotic stellar populations such as blue straggler stars (BSSs), yellow straggler stars (YSSs), and cataclysmic variables. These systems, as well as the end products of stellar evolution, such as hot white dwarfs (WDs), emit the bulk of their energy in the ultraviolet (UV) regime. UV observations of OCs are crucial to detect and understand the properties of hot stellar populations, as highlighted by Landsman et al. (1997) and Knigge et al. (2008).

One of the intriguing products of stellar interactions in OCs are BSSs whose origin and evolution are still debated (Boffin et al. 2015). As these stars appear brighter and bluer than the stars located in the main-sequence turn-off (MSTO) region of the cluster’s color–magnitude diagram (CMD), they are expected to be more massive than TO stars. To explain the mass gain and rejuvenation of these objects, the main formation scenarios proposed are direct collisions or spiraling in of binary stars resulting from mergers (Hills & Day 1976), or mass-transfer activity in close-binary systems (McCrea 1964). The dynamical evolution of hierarchical triple systems leading to

the merger of an inner binary via the Kozai mechanism (Iben & Tutukov 1999; Perets & Fabrycky 2009) is another possible mechanism. Observational studies of BSSs suggest that a combination of all the formation channels are prevalent, which have a dependence on their environment, as they are found in a variety of stellar environments such as OCs (de Marchi et al. 2006; Ahumada & Lapasset 2007), globular clusters (GCs) (Ferraro et al. 2012), the Galactic field (Santucci et al. 2015), and dwarf galaxies (Santana et al. 2012). Thus, studying BSSs can provide information about the dynamical history of the cluster, the role of dynamics on binary evolution, the frequency of binary systems, and the contribution of binaries to cluster evolution. Member stars that are redder than the BSSs and brighter than the subgiants found in the CMDs of OCs and GCs are considered as evolved BSSs, and are known as YSSs (see Sindhu et al. 2018 and references therein).

There are only a few OCs in our galaxy known to harbor planetary nebulae (PNe). PNe are classically considered to represent the late stages in the stellar evolution of all low-mass as well as intermediate-mass stars with a mass range of $0.8\text{--}8 M_{\odot}$ (Weidemann 2000). As the evolutionary lifetimes of PNe are short (around $10^3\text{--}10^5$ yr, depending on the mass of the progenitor) when compared to other evolutionary phases, especially when the number of evolved stars present in OCs are small, PNe as members of OCs are rare and are not expected in young OCs. Objects in this short-lived phase are critically important to our understanding of the physical processes and steps that transform stars into their remnants. They allow us to test the theory of stellar evolution, including the physics of nucleosynthesis and the relation between a star’s initial mass and its WD remnant (Kwitter et al. 2014). Moreover, the



Original content from this work may be used under the terms of the [Creative Commons Attribution 4.0 licence](https://creativecommons.org/licenses/by/4.0/). Any further distribution of this work must maintain attribution to the author(s) and the title of the work, journal citation and DOI.

chemical composition of PNe can provide information about the dredge-up of chemical elements, which is expected to depend on the star’s initial mass and composition. Finding a planetary nebula (PN) as a member of an OC gives us an excellent opportunity to characterize and constrain its crucial parameters, such as distance, reddening, and age.

NGC 2818, has the unique distinction of being one of two galactic OCs probably associated with a PN, and interestingly, the name NGC 2818 is assigned to both an OC and a PN. Most importantly, the membership of the PN to the OC is still debated. In this study, we analyse both the cluster and the PN, NGC 2818.

Here we present the results of the UV imaging of NGC 2818 (both PN and OC) in four far-UV (FUV) filters using the Ultra Violet Imaging Telescope (UVIT) on AstroSat. Our main aims are (1) to identify and characterize the BSSs and YSSs in the cluster to shed light on their formation and evolution and (2) to characterize the central star of the PN (CSPN) to investigate its association with the cluster. The age of this cluster is estimated to be ~ 800 Myr, and the reddening of the cluster is $E(B - V) = 0.2$ mag (Sun et al. 2021). This cluster is located at a distance of 3250 ± 300 pc and its metallicity is found to be solar (Sun et al. 2021).

NGC 2818 is one of the OCs that shows an extended main-sequence turn-off (eMSTO) phenomenon (Bastian et al. 2018), where the cluster’s MS is extended in the CMD more than what is expected from a simple stellar population with a conventional evolutionary history. It has been demonstrated that stellar rotation is the most probable cause of this phenomenon (Bastian & de Mink 2009; Brandt & Huang 2015; Niederhofer et al. 2015; Cabrera-Ziri et al. 2016; Gossage et al. 2019). A spectroscopic study by Bastian et al. (2018) showed that, in NGC 2818, stellar rotation is indeed linked to the stars’ positions on the MSTO of the CMD made using Gaia magnitudes (G) and color ($G_{bp} - G_{rp}$), such that rapidly rotating stars preferentially lie on the red side of the eMSTO. However, the color range ($G_{bp} - G_{rp}$) in optical CMD is relatively small, whereas a larger color range is seen in UV colors, which is expected as rotational effects are more prominently displayed in UV colors mainly because of their sensitivity to surface (effective) temperature changes. This study also explores the correlation between the colors derived from UVIT FUV filters and stellar rotation.

The layout of this paper is as follows. In Section 2, we describe the observations, data reduction, and analysis methods. In Section 3, we present proper-motion-based membership information using Gaia Early Data Release 3 (EDR3) data for cluster stars and the PN. Section 4 presents the selection of BSSs and YSSs from the observed UV and optical CMDs, including the stellar rotation effects on CMDs. In Sections 5 and 6, we describe the properties of the BSSs and YSSs derived from the UVIT photometry along with GALEX, Gaia, and ground-based photometry, and their evolutionary statuses. A detailed discussion of all results is provided in Section 7. Finally, in Section 8, we summarize our main results and conclusions.

2. Observational Data and Analysis

2.1. UVIT Data

In order to probe the nature of the exotic stellar populations in NGC 2818, we use data acquired with the UVIT instrument

Table 1
List of the FUV Observations of NGC 2818 Obtained with UVIT in the Two Epochs Used in This Work

Filter	λ_{mean} (Å)	$\Delta\lambda$ (Å)	ZP (AB mag)	t_{exp} (s)		A_{λ} (mag)
				(1st epoch)	(2nd epoch)	
F148W	1481	500	18.09	...	1736	1.58
F154W	1541	380	17.77	1491	2877	1.55
F169M	1608	290	17.41	1715	1999	1.54
F172M	1717	125	16.27	1903	2878	1.51

Note. The last column lists the extinction value computed in each FUV filter using Fitzpatrick (1999)’s law of extinction.

on board the Indian multiwavelength astronomy satellite AstroSat. UVIT produces images of the sky in FUV, near-UV (NUV), and visible, simultaneously, over a circular field-of-view of $28'$ diameter with a spatial resolution of $\sim 1''.5$ in both the FUV and NUV channels. More details about the telescope, its initial and new calibration, and its results are described in detail by Tandon et al. (2017, 2020). The derived magnitudes of the stellar sources observed with the UVIT filters are in the AB magnitude system.

The observations of NGC 2818 used in this work were made in two epochs, first on 2018 December 21 (Prop: A05_196 –P. I: N. K. Rao), and the second on 2020 June 11 (Prop: A09_047 –P.I: N. K. Rao). In the first epoch, the observations were carried out in three FUV filters (F154W, F169M, and F172M), and in the second, observations were performed with deep exposures in four FUV filters (F148W, F154W, F169M, and F172M). The observations were carried out in several orbits in order to complete the allotted exposure times in the given filters. We utilize a customized software package, CCDLAB (Postma & Leahy 2017), to correct for geometric distortion, flat field, and spacecraft drift and create images for each orbit. Then, the orbit-wise images were co-aligned and combined to generate science-ready images in order to get a better signal-to-noise ratio. Further analysis was done using these final science-ready images to obtain the magnitudes of the sources detected with UVIT. The details of the UVIT observations of NGC 2818 used in this analysis are tabulated in Table 1. In Figure 1, we show the UVIT image of the cluster taken in the FUV F148W band where the orange color depicts the FUV detections. This image exhibits an extended structure displaying the beautiful PN NGC 2818, where the central star can be seen in the FUV. In Figure 2, we present UVIT images of a PN in three different FUV filters: F154W, F169M, and F172M, with blue color denoting the FUV emission and the central star is clearly visible.

2.2. Photometry

To extract the magnitudes of the detected stars in all FUV images, we have carried out point-spread function (PSF) photometry using the IRAF/NOAO package DAOPHOT (Stetson 1987). The steps taken to obtain the magnitudes of the sources are as follows: first, the stars are located in the image using the DAOFIND task in IRAF. Further, we used the PHOT task to perform aperture photometry. To construct the model PSF using the PSF task, bright and isolated stars are selected in the image using the PSTSELECT task. The average PSF of the stars in all FUV images is $\sim 1''.2$. The ALLSTAR task is used to fit the model PSF to all the detected stars in the

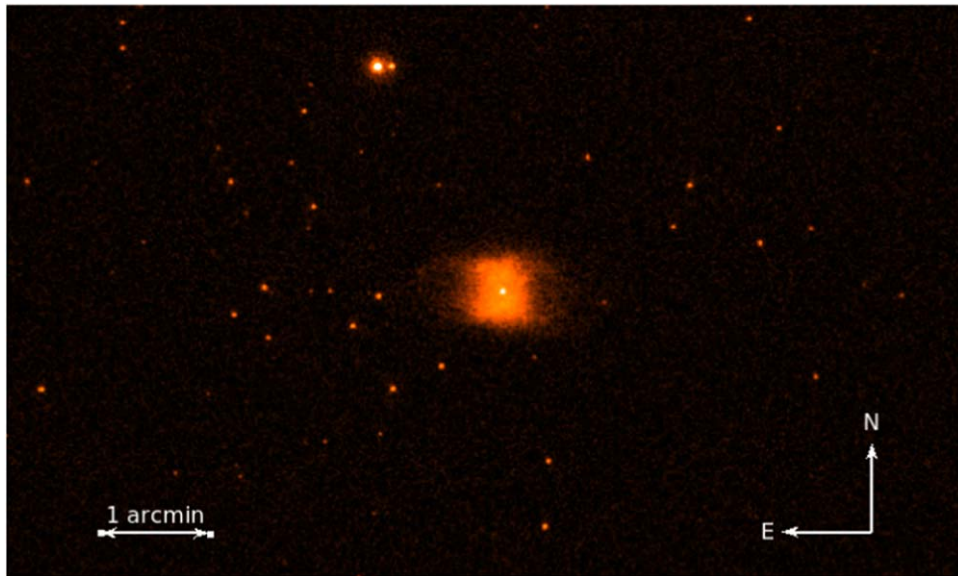


Figure 1. UVIT color image of the OC NGC 2818 in the FUV F148W channel. Here the orange color depicts the FUV detections. The extended structure in this image represents the PN NGC 2818. North is up, and east is left in the image.

image to obtain the PSF-fitted magnitudes. The PSF magnitudes were converted to aperture photometry scale using the PSF correction further followed by aperture correction, estimated using a curve of growth analysis by choosing isolated bright stars in the field. Finally, the saturation correction, in order to account for more than one photon per frame, was applied to the obtained magnitudes in UVIT filters. All steps to perform the saturation correction are described in detail by Tandon et al. (2017). The extracted instrumental magnitudes are calibrated into the AB magnitude system using the zero-points (ZPs) reported in the recently published calibration paper (Tandon et al. 2020). Figure 3 shows the PSF-fit error (median) as a function of magnitude in the four FUV filters for the observations. We have detected stars up to ~ 22 mag with PSF-fit errors less than 0.3 mag in all FUV filters and considered them for further analysis in the paper.

To apply an extinction and reddening correction to the derived UVIT magnitudes of all detected stars, we adopted the reddening $E(B-V) = 0.2$ mag mentioned by Sun et al. (2021). The ratio of the total-to-selective extinction, $R_V = 3.1$ for the Milky Way, was taken from Whitford (1958) to calculate the extinction value in the visual band (A_V). We used the Fitzpatrick extinction law (Fitzpatrick 1999) to compute the extinction coefficients A_λ for all UVIT filters, as listed in Table 1.

2.3. Other Catalogs

This cluster was previously observed in UV, optical, and infrared (IR) all-sky surveys with GALEX (Bianchi et al. 2017), SDSS (Alam et al. 2015), APASS (Henden et al. 2015), 2MASS (Cutri et al. 2003), and WISE (Cutri et al. 2021), respectively. In this work, we combined the UVIT data with the multiwavelength photometric catalog spanning a wavelength range from UV–IR. We used the virtual observatory tool in VOSA to cross-match the UVIT-detected sources with the abovementioned photometric catalogs (Bayo et al. 2008).

3. Membership Determination

We employed the Gaia EDR3 catalog that provides data with unprecedented precision to identify the cluster members. In particular, it provides the complete five-parameter astrometric solution (positions, proper motions (PMs), and parallaxes) and magnitudes in its three photometric bands (G , G_{BP} , and G_{RP}) with a limiting magnitude of about $G \sim 21$ mag. To assign the PM membership probability (MP; P_μ) of all stars observed in the cluster, we first downloaded all detections located within a $30'$ radius from the cluster's center. To include all possible members of the cluster, we opted to use a radius bigger than that provided by Kharchenko et al. (2013)'s catalog. Then, we applied data quality criteria to select sources with a good astrometric solution. Stars are selected as follows: (i) we removed those with parallaxes that deviate by more than 3σ from the expected parallax calculated using the previously known distance to the cluster, where σ is the error in parallax given in the Gaia EDR3 catalog, (ii) we also removed sources with a renormalized unit weight error (RUWE) exceeding 1.2 as larger values of this parameter might lead to an unreliable astrometric solution (Lindgren et al. 2018; Riello et al. 2021).

We made use of a probabilistic Gaussian mixture model (GMM) method to select cluster members and infer the intrinsic parameters of the distributions of both member and nonmember stars. In this method, the distribution of sources in the vector point diagram (VPD) (μ_α , μ_δ) is modeled as a mixture of two Gaussian distributions, one for the cluster members and another one for the field sources. The details of this method are well described by Vasiliev (2019). The Gaussian probability distribution corresponding to the sum of two distributions is

$$f\left(\mu|\bar{\mu}_i, \sum_i\right) = \sum_{i=1}^2 w_i \frac{\exp\left[-1/2(\mu - \bar{\mu}_i)^T \Sigma_i^{-1}(\mu - \bar{\mu}_i)\right]}{2\pi\sqrt{\det \Sigma_i}}, \quad (1)$$

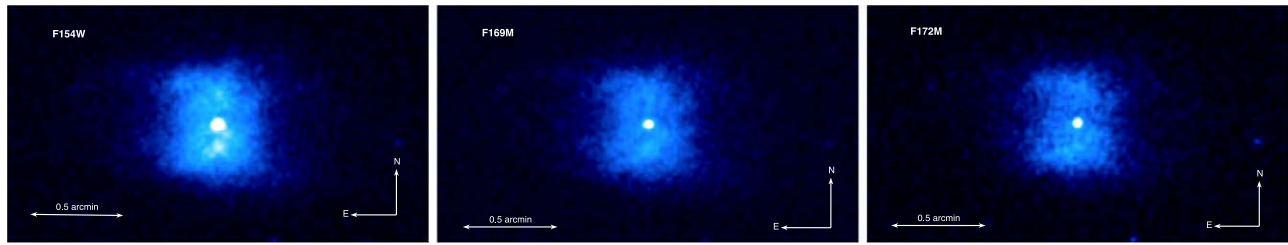


Figure 2. UVIT/FUV images of the PN NGC 2818 in three filters: F154W, F169M, and F172M.

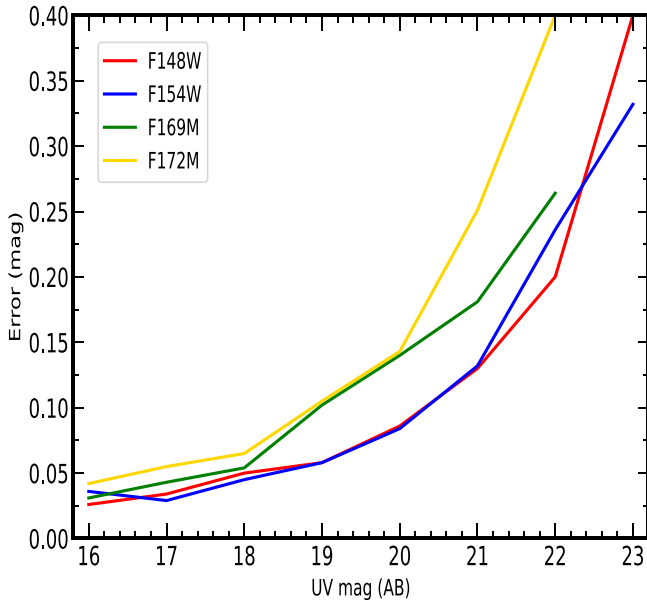


Figure 3. PSF-fit errors (median) as a function of magnitude for our UVIT observations of NGC 2818 in all FUV bandpasses.

$$w_i \geq 0, \sum_{i=1}^2 w_i = 1, \quad (2)$$

where μ is an individual PM vector, $\bar{\mu}_i$ is the field and cluster mean PM, Σ is the symmetric covariance matrix, and w_i contains the weights for the two Gaussian distributions. Full details of this method for the n-dimensional case are described by Vasiliev (2019).

The initial guesses for the cluster’s PM μ_α and μ_δ values and internal velocity dispersion are taken from Cantat-Gaudin et al. (2020). We utilized GaiaTools³ to maximize the total log-likelihood of the GMM and measure the mean PM and standard deviation of both Gaussian distributions. The MPs of all the selected stars are calculated using the same technique simultaneously. The equations used to maximize the log-likelihood of the GMM and estimate the MP of the i^{th} star belonging to the k^{th} component are given in Appendix A of Vasiliev (2019).

The PM mean and standard deviations of the cluster distribution are computed to be $\mu_\alpha = -4.417 \text{ mas yr}^{-1}$ and $\mu_\delta = 4.540 \text{ mas yr}^{-1}$, with $\sigma_c = 0.045 \text{ mas yr}^{-1}$. In Figure 4, we show the positions of stars in the sky, in a PM space known as a VPD, and in an optical CMD created using Gaia filters. The cyan dots in all the plots depict the member stars belonging to the cluster, and the black dots represent field stars. 718 stars are

identified as most likely cluster members with $P_\mu > 50\%$ and are considered for subsequent analysis. This method works well for distinguishable distributions of PMs for field and cluster stars in a VPD. But, in this case, the PMs of the cluster stars are located well within the PM distribution of the field stars, suggesting a nontrivial identification of cluster members from field stars. Therefore, it is possible that stars with a lower MP than the abovementioned limit might also be members of the cluster.

3.1. Is the PN a Member of the Cluster?

The membership of the PN with OC has been debated in several studies in the past. Tiffet et al. (1972) found that PN NGC 2818 is a member of the OC of the same name. Dufour (1984) presented the results of photometric as well as spectroscopic observations of the nebula to analyse its physical properties and chemical composition. He suggested that the nebula is probably associated with the star cluster. Pedreros (1989) analysed this cluster using CCD *UBV* photometric data and assumed a physical association of the nebula with the cluster. Surendiranath et al. (1990) also suggested the association of the PN with the cluster from their CCD photometry of the cluster. However, Mermilliod et al. (2001) derived accurate heliocentric radial velocities (RVs) for 12 cluster red giants to obtain a mean heliocentric RV of $V_{\text{hel}} = +20.7 \pm 0.3 \text{ km s}^{-1}$, significantly different from the PN’s velocity of $-1 \pm 3 \text{ km s}^{-1}$ (Meatheringham et al. 1988), suggesting that they are unrelated. Recently, (Vázquez 2012) reanalyzed the complex kinematics and morphology of the nebula using high-resolution Hubble Space Telescope (HST) archive imaging and high-dispersion spectroscopic data and determined the systemic heliocentric velocity of the PN to be $+26 \pm 2 \text{ km s}^{-1}$ in closer agreement with the OC, suggesting its membership. Moreover, based on its RV, $H\alpha$ surface brightness, and radius, Frew et al. (2016) concluded that the PN might be a cluster member.

The Gaia EDR3 trigonometric parallax for the CSPN is $0.0319 \pm 0.21 \text{ mas}$, but it can be noted that the uncertainty in it is more than its value. So, it cannot be used to obtain the distance to the nebula. The best estimate of the statistical distance is given by Frew et al. (2016) as $3000 \pm 800 \text{ pc}$, not too far from cluster distance of $3250 \pm 300 \text{ pc}$ estimated by Sun et al. (2021). Cantat-Gaudin et al. (2020) and Cantat-Gaudin & Anders (2020) obtained the members of several OCs, including NGC 2818, using Gaia DR2 PM data, and suggested that it is a nonmember of the cluster.

In our membership analysis, we have obtained the membership of the CSPN using Gaia EDR3 PM data. The PM in R.A. and decl. of the CSPN as listed in the Gaia EDR3 catalog is $\mu_\alpha = -3.712 \pm 0.185 \text{ mas yr}^{-1}$ and $\mu_\delta = 4.94 \pm 0.18 \text{ mas yr}^{-1}$. Its P_μ is estimated to be $\sim 11\%$, indicating nonmembership.

³ <https://github.com/GalacticDynamics-Oxford/GaiaTools>

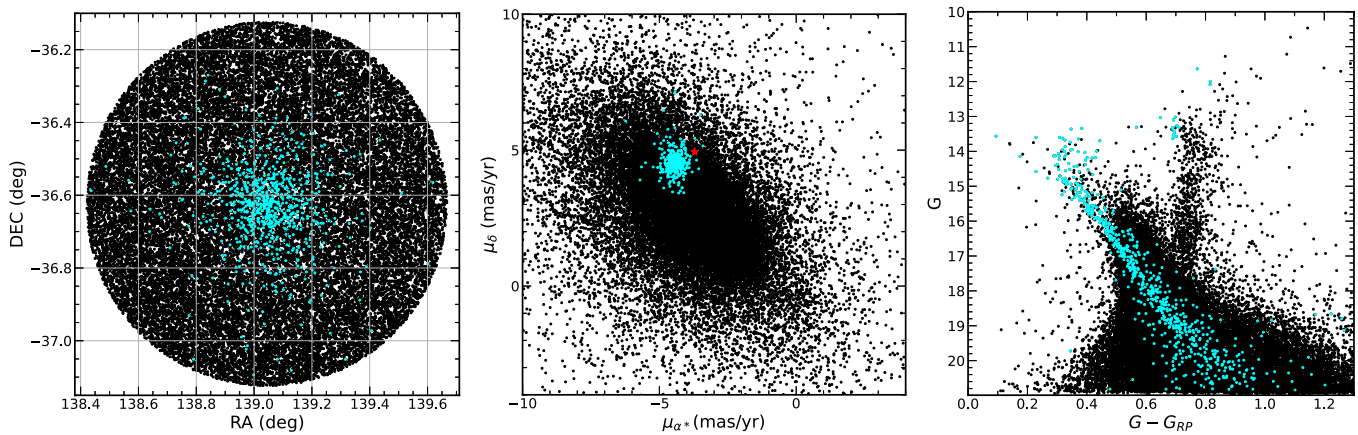


Figure 4. In three panels from left to right, PM members of the cluster are shown with cyan dots, and the remaining Gaia EDR3 sample is marked with black dots, representing field stars. Left panel: position in the sky; middle panel: VPD; and right panel: Gaia optical CMD.

Nevertheless, it can be noted from the location of the CSPN shown with the red star symbol in the VPD that it is lying close to the PM distribution of the cluster members (cyan dots), implying that it is quite likely a member of the cluster. Statistically, it is lying within 3σ of the mean PM of the cluster. We expect that the future Gaia data release (Gaia DR4) might give more precise and accurate PM measurements that can reconfirm its association with the cluster. Further, assuming that both the cluster and nebula are at the same distance, we computed their true velocity using their available RV and PM information. We found that the true velocity of the cluster and nebula turn out to be approximately the same ($V_C = 99.7 \text{ km s}^{-1}$ and $V_{PN} = 98.7 \text{ km s}^{-1}$, respectively), implying that their space velocities are similar.

3.1.1. Reddening Toward the PN

Several estimates of extinction/reddening toward the cluster have been made since the initial investigation by Tifft et al. (1972) who found $E(B-V)$ of 0.22 mag, reconfirmed by Surendiranath et al. (1990) and recently refined by Sun et al. (2021), to 0.20 mag. However, there are a few independent estimates of extinction toward the PN NGC 2818. Dufour (1984) estimated it from the Balmer line $H\alpha/H\beta$ ratio as 0.24 ± 0.02 mag. Gathier & Pottasch (1988) list a value of 0.20 mag, and Frew et al. (2016) estimated a value of 0.17 ± 0.08 mag. We presently estimate an $E(B-V)$ value using free-free continuum flux and the nebular $H\beta$ flux. The flux density, S_ν , at 5 GHz of the entire nebula is measured by Zhang (1995) as 33 mJy. The total $H\beta$ flux is estimated by Gathier & Pottasch (1988) as $\log F(H\beta)$ as -11.40 ($\text{erg cm}^{-2} \text{ s}^{-1}$). Following Pottasch (1984), the expected ratio of S_ν to $F(H\beta)$ is given as

$$\frac{S_\nu}{F(H\beta)} = 2.51 \times 10^7 \times T_e^{0.53} \times (\nu)^{-0.1} \times Y \text{ Jy erg}^{-1} \text{ cm}^{-2} \text{ s}^{-1},$$

where T_e is the electron temperature, ν is the frequency in GHz, and $Y = (1 + \frac{n(\text{He}^+)}{n(\text{H}^+)})$. The value of $\frac{n(\text{He}^+)}{n(\text{H}^+)}$ is ~ 0.13 assuming all He is in He^+ form. Dufour (1984) derived a $T_e[\text{OIII}]$ of $14,500 \pm 500$ K. From the above relation, the $\log F(H\beta)$ expected from the radio continuum is -11.07 . The equation from Milne & Aller (1975) used to compute the

reddening is as follows

$$E(B-V) = \frac{1}{1.46} \log \frac{F(H\beta)_{\text{exp}}}{F(H\beta)_{\text{obs}}}.$$

Inserting the expected and observed $\log F(H\beta)$ values in the above equation, we obtain a value of $E(B-V) \sim 0.23$ mag. Thus, the extinction/reddening toward this cluster and nebula are of similar values.

From the comparisons of distance, RV, PM, and extinction/reddening values of the cluster and nebula, we suggest a physical association of the PN with the OC.

4. CMDs

4.1. Classification of Exotic Sources

This section describes the classification and identification of exotic sources, such as BSSs and YSSs, expected to emit in the FUV. As mentioned in Section 3, we considered probable cluster members with $P_\mu > 50\%$ and created a PM-cleaned optical CMD ($G_{\text{pp}} - G_{\text{rp}}$ versus G) using the Gaia filters shown in Figure 5. In this CMD, stars outlined in cyan depict the various identified star populations in the FUV images. Rain et al. (2021) presented a new PM-cleaned catalog of BSSs in galactic OCs using Gaia DR2 data. We cross-matched the Gaia EDR3 cluster members with their BSS catalog to classify this population in the cluster. Out of the five BSSs in NGC 2818 identified by Rain et al. (2021), we detected four BSSs. The remaining one BSS, not detected by us, is found to be a nonmember of the cluster in our membership catalog and also falls outside the FoV of NGC 2818 observed with UVIT in two epochs. Jadhav & Subramaniam (2021) also produced a catalog of BSSs in OCs using Gaia DR2 data with a $P_\mu > 70\%$, and they found two BSS candidates in this cluster. The differences in the abovementioned catalogs could be due to the adopted age criteria, selection methods, and different MP cutoffs used in the two studies.

We obtained MESA Isochrones and Stellar Tracks (MISTs) for the UVIT and Gaia EDR3 filters from an updated MIST online database⁴ to identify and classify distinct evolutionary sequences in the cluster (Choi et al. 2016; Paxton et al. 2018). We considered isochrones with $[\alpha/\text{Fe}] = +0.0$ and a metallicity of $Z = 0.017210$ (Sun et al. 2021), not incorporating initial rotation. Cluster parameters such as age, extinction, and

⁴ https://waps.cfa.harvard.edu/MIST/interp_isos.html

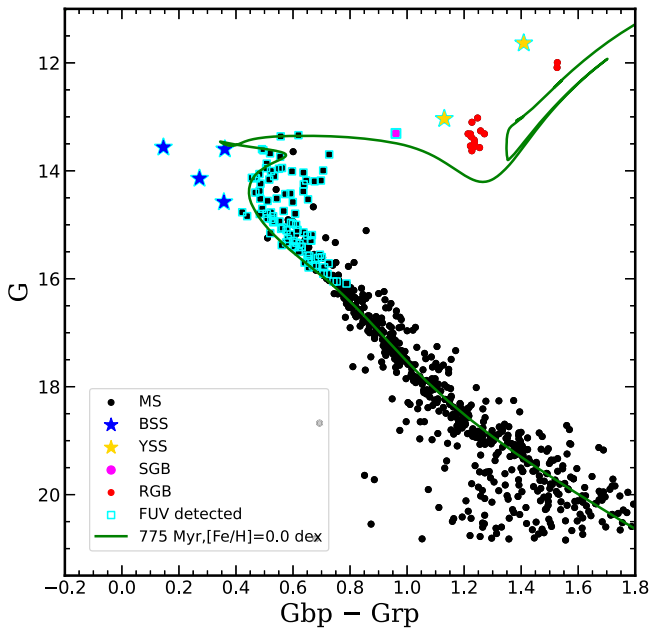


Figure 5. Optical CMD of the NGC 2818, created using Gaia EDR3 photometry. All filled symbols denote stars with $P_{\mu} \geq 50\%$. Blue-filled stars and yellow-filled stars are the selected BSSs and YSSs used for further cross-matching with the UVIT data, respectively. The stars detected in all FUV images are outlined with cyan-colored squares and star symbols. The overlaid green solid line represents the nonrotating MIST isochrone of solar metallicity and an age of 775 Myr, set at a reddening of $E(B-V) = 0.2$ mag and a distance modulus of $(m-M)_V = 12.56$ mag.

distance modulus, adopted to fit the isochrone to the observed optical CMD, are 775 Myr, $A_V = 0.6$ mag, and $(m-M)_V = 12.56$, respectively (Sun et al. 2021). The isochrone (solid green line) overlaid in the observed optical CMD is displayed in Figure 5. We notice that the isochrone appears well-matched to the observed CMD along the MS subgiant branch (SGB), but it is not reproducing the observed position of the red clump. To account for this mismatch along the red clump, (Bastian et al. 2018) suggested that there might be a problem in the calibration of the models for red clumps or the conversion between the theoretical properties of the isochrones (temperature, gravity, and luminosity) to the observational space in Gaia filters is off.

We also selected the YSSs based on their location in the optical CMD, as they have colors in between the TO and RGB and appear brighter than the SGB. We have chosen two such stars marked with yellow colored filled symbols shown in Figure 5.

4.2. FUV–Optical CMDs

This section presents the FUV–optical CMDs generated by cross-identifying common stars between the optical and our FUV detections. We cross-matched the sources detected in the UVIT FUV filters with Gaia EDR3 with a maximum separation of $1''.3$, which is the typical FWHM of the PSF for the UVIT filters. To plot the FUV–optical CMDs, first, we made the magnitude system adopted by Gaia similar to that of UVIT. That is, we transformed the Vega magnitude system used in the Gaia photometric system to the AB system using the photometric ZPs reported in the Gaia EDR3 documentation.⁵

We have created and shown the FUV–optical CMDs for cluster members in Figure 6 using the F148W and F169M filters. We note that a similar trend of detected stellar populations is observed in the other two filters (F154W & F172M). The error bars displayed in all FUV CMDs are estimated as the median of the stars’ errors at a chosen magnitude range. The FUV–optical CMDs are also overlaid with updated MIST isochrones (Choi et al. 2016) to compare the locations of the distinct sequences predicted by the theoretical models with the observed ones. In all FUV images, hot and bright stars such as BSSs, YSSs, and MS are detected. We have detected four BSSs out of five previously known in the literature (Rain et al. 2021). Four detected BSSs are confirmed RV and PM members. Two YSSs are also identified in all FUV images. We note that these stars are well-separated and brighter than the theoretical isochrone presenting the SGB sequence in all FUV–optical CMDs, in turn confirming their classification as YSSs. RGB and red clump stars are too faint to be detected in the FUV.

The FUV–optical CMDs show a large scatter along the MS, as shown in Figure 6, unlike the optical CMDs. The overlaid isochrones in all FUV–optical CMDs help to trace the MS scatter. We note that a few MS stars are brighter than theoretical MSTO not reproduced by the isochrones. These might have high rotational velocities, accounting for this feature. Some of them may be binaries or potential BSSs. One BSS is found to be very hot and bright in all FUV–optical CMDs compared to the other three BSSs. This BSS can be an exciting candidate to characterize, as it might have a hot WD companion. As two YSSs are detected in all FUV images and found to be bright in all FUV–optical CMDs, these stars also might have a hot companion, which leads to their detection in the FUV images. Thus, these are intriguing targets to understand further in terms of their formation and evolution in the cluster.

4.3. eMSTO in FUV CMDs

In order to check the sensitivity of the UVIT colors to the T_{eff} affected by the rotational velocity, we plot $(G_{\text{bp}} - G_{\text{rp}})$ versus $(F172M - G)$ color as shown in Figure 7, which indicates a linear relation. The range of Gaia color is only 0.4 mag whereas $(F172M - G)$ spans about 3.0 mag, which makes the $(F172M - G)$ color more sensitive and responsive to rotational velocity. The $(F172M - G)$ color is preferred over $(F169M - G)$ because the band F172M allows only continuum light, and no chromospheric or transitional emission lines are seen in late-type stars in the FUV.

When comparing the CMDs, $(F172M - G)$ versus G_{bp} (Figure 8, upper right) with the CMD of $(G_{\text{bp}} - G_{\text{rp}})$ versus G_{bp} (Figure 8, upper left) shows the sensitivity of the $(F172M - G)$ color. The bend in the isochrone in $(F172M - G)$ versus the G_{bp} CMD at a color of 4.0 indicates the beginning of the eMSTO prominently (unlike Figure 8, left panel), and all the stars right of the isochrone show high rotational velocities. The MS comprises stars with both high and low rotational velocities. However, the CMD of $(F169M - G)$ versus G_{bp} exhibits some more aspects. From the comparison of the $(F169M - G)$ color with $(F172M - G)$ in Figure 8, we find that the former is redder than the latter. It can be due to the fact that the F169M flux in late-type stars is smaller than at F172M. Moreover, the predicted colors using the theoretical isochrones are following the same trend.

⁵ <https://gea.esac.esa.int/archive/documentation>

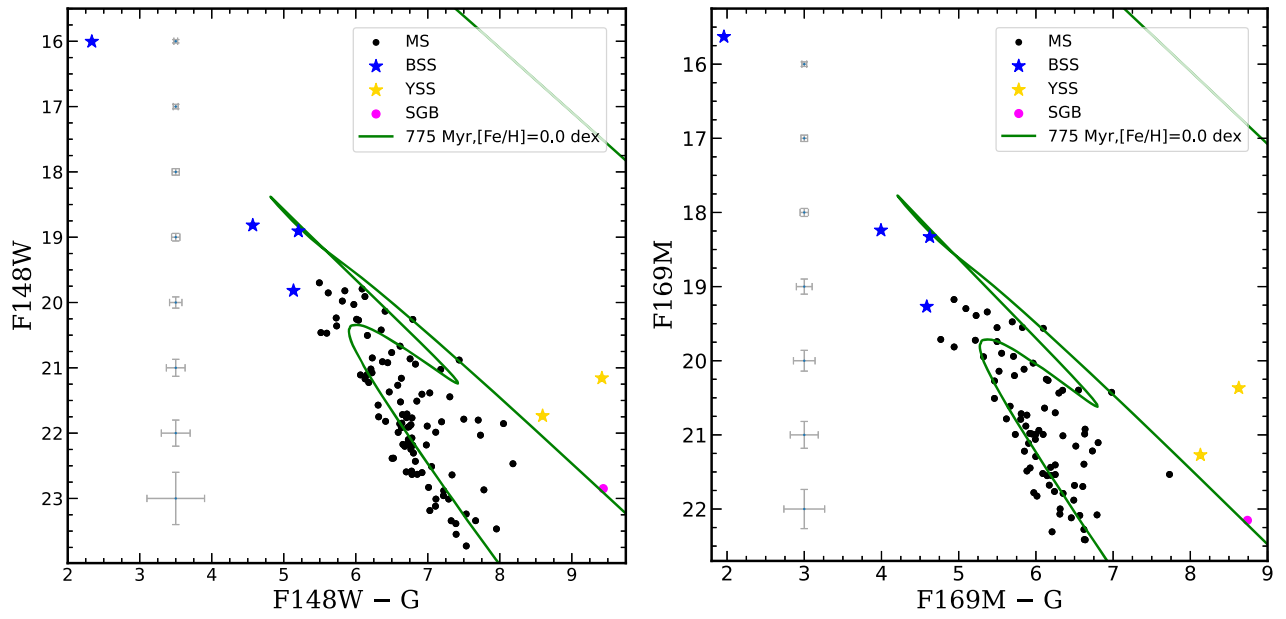


Figure 6. FUV-optical CMDs using the F148W and F169M passbands of NGC 2818 of confirmed members cross-identified using the UVIT FUV magnitudes and the Gaia EDR3 catalog. The error bars (median) are shown in gray color on the left side of each panel. The rest of the details are the same as in Figure 5.

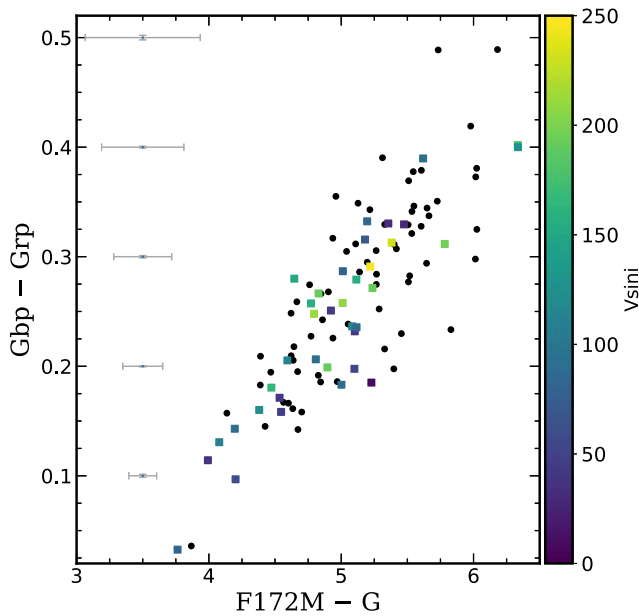


Figure 7. (F172M-G) vs. ($G_{bp}-G_{rp}$) color-color plots of all stars detected with UVIT color-coded by their measured $V_{\text{sin } i}$ values. Stars with black color symbols do not have estimated $V_{\text{sin } i}$ values.

It is well known that MS stars later than about F2 possess coronal and transitional regions as evidenced in the FUV region by emission lines of C IV, He II, Si IV, N V, N IV, etc. (Linsky & Haisch 1979; Jordan & Linsky 1987). Prominent lines like C IV and He II occur in the F169M band region (unlike the F172M band). F154W and F148W should contain a few more emission lines in addition to C IV and He II. Thus, the CMD of (F169M-G) versus G_{bp} shows that the MS stars are shifted bluewards to the isochrone, probably suggesting the presence of transitional region lines. Even in the (F169M-F172M) versus G_{bp} CMD shown in the lower right panel of Figure 8, it is evident that most stars have bluer colors than the

theoretically expected ones from isochrones. It is to be noted that all stars on the blue edge of the MS in the CMD of (F169M-G) versus G_{bp} ($15 < G_{bp} < 16$; $5 < (F169M-G) < 6$) show high rotational velocity in contrast to the CMD of (F172M-G) versus G_{bp} ($15 < G_{bp} < 16$; $4 < (F172M-G) < 5$). It is fairly well established that high rotational velocities enhance coronal and transitional line emissions (Pallavicini et al. 1981; Linsky et al. 2020). Thus, it is consistent with the suggestion that high rotation stars are on the blue side because of high emission line activity in total contrast to the MS of the (F172M-G) versus G_{bp} CMD. This phenomenon sets into stars redder than ($G_{bp}-G_{rp}$) ~ 0.5 mag.

5. SED Fits

It is well demonstrated in previous studies of exotic stellar populations, such as BSSs in OCS, that they are the products of stellar interactions. There might be a chance of detecting a binary companion in the case of BSSs and YSSs. Spectral energy distributions (SEDs) of such systems can be used to obtain the parameters of the multiple components. In this section, we present the multiwavelength SEDs constructed for the BSSs, YSSs, and CSPN identified with UVIT to derive their atmospheric parameters like effective temperature (T_{eff}), luminosity (L), and radius (R). We aim to probe the physical nature of these stars and probable hot companions, if present, by estimating their stellar parameters and placing them on the H-R diagram. SEDs are generated with the observed photometric data points spanning a wavelength range from FUV-IR and fitted with selected theoretical models. We made use of the virtual observatory tool, VOSA (VO Sed Analyzer; Bayo et al. 2008) for the SED analysis. The details of the SED-fitting technique are described by Rani et al. (2021). In addition to χ_{red}^2 , VOSA calculates two extra parameters, Vg_f and Vg_{f_b} , known as modified χ_{red}^2 to estimate the goodness of fit in case the observational flux errors are too small. The value of Vg_{f_b} should be less than 15 to achieve a reliable SED fit (Rebassa-Mansergas et al. 2021).

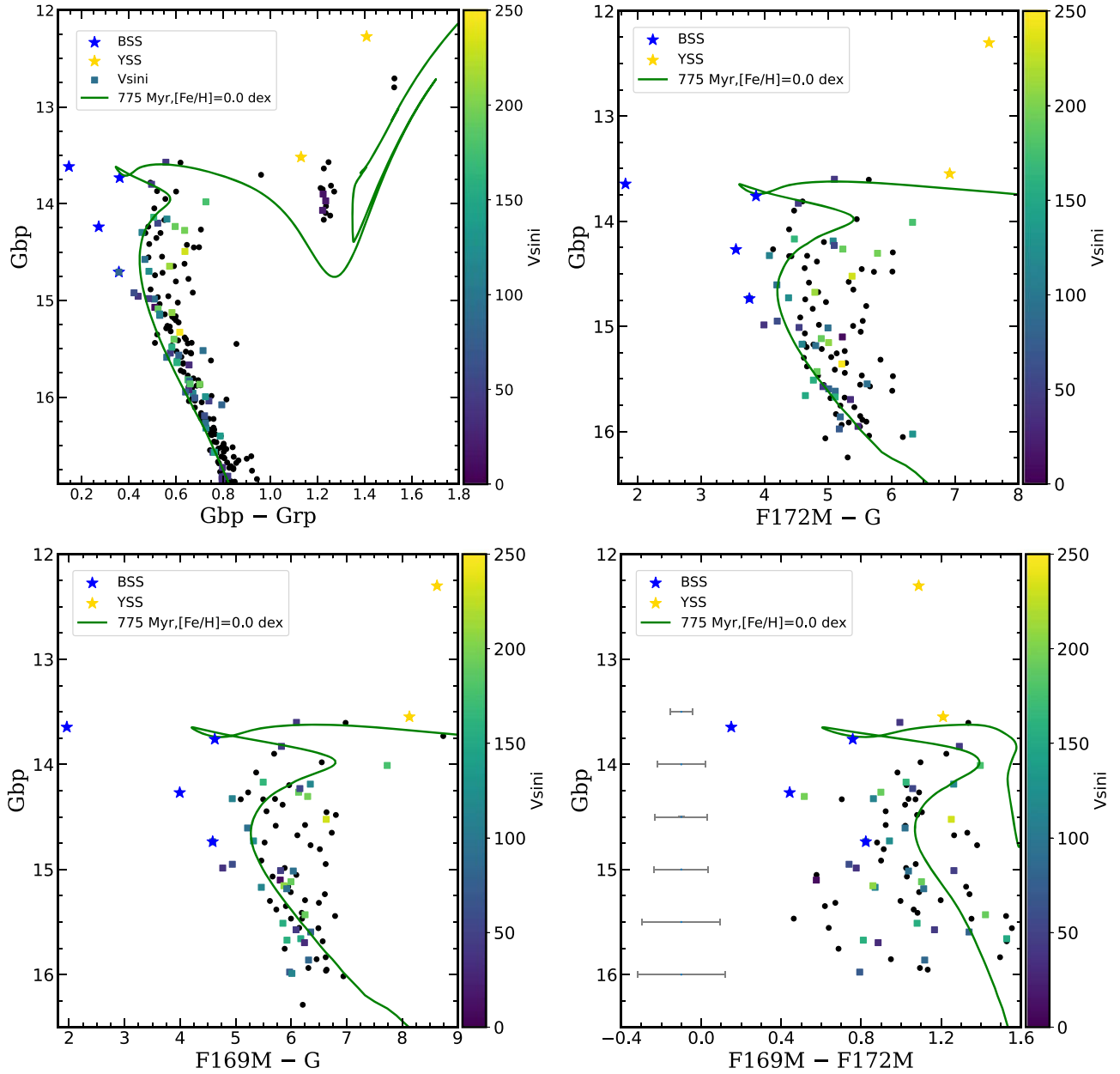


Figure 8. Optical (upper left), (F172M–G) vs. G_{bp} (upper right), (F169M–G) vs. G_{bp} (lower left), and (F169M–F172M) vs. G_{bp} (lower right) CMDs of NGC 2818 members color-coded by measured V_{sini} values. The rest of the details are the same as in Figure 5.

Kurucz stellar atmospheric models are employed to create the synthetic SEDs (Castelli et al. 1997; Castelli & Kurucz 2003) for the BSSs and YSSs, which have observed photometric data points covering a wavelength range from UV to IR. The free parameters available in the Kurucz model are T_{eff} , metallicity, and $\log g$. To fit the observed SEDs of the stars, as mentioned earlier with Kurucz models, we assumed T_{eff} and $\log g$ as free parameters, and fixed the value of the metallicity to $[\text{Fe}/\text{H}] = 0.0$, close to the cluster’s metallicity. We adopted the range of T_{eff} from 5000 to 50,000 K and $\log g$ from 3.5 to 5 dex in the Kurucz models. We combined the photometric data points of UVIT (four passbands) with GALEX (two passbands), Gaia EDR3 (three passbands) (Gaia Collaboration et al. 2018), SDSS (three passbands), APASS (two passbands), 2MASS (three passbands), and WISE (four passbands) to generate the observed SEDs. VOSA makes use of the Fitzpatrick reddening law (Fitzpatrick 1999; Indebetouw et al.

2005) to compute the extinction in the different passbands and correct for extinction in observed fluxes for the provided A_V . VOSA utilizes a Markov Chain Monte Carlo (MCMC) approach to estimate the uncertainties in the stellar atmospheric parameters obtained using the SED fit. We estimated the radius (R) of the star using the scaling relation $M_d = \left(\frac{R}{D}\right)^2$, where D is the distance to the cluster and M_d is the scaling factor.

We conducted an SED-fitting analysis for four BSSs, two YSSs, and PN, as described in the following subsections.

5.1. BSSs

The best-fitted SEDs for all BSSs are shown in Figure 9, where the lower panel of each SED depicts the fractional residuals between the observed and predicted fluxes. The overplotted black solid line presents the synthetic Kurucz

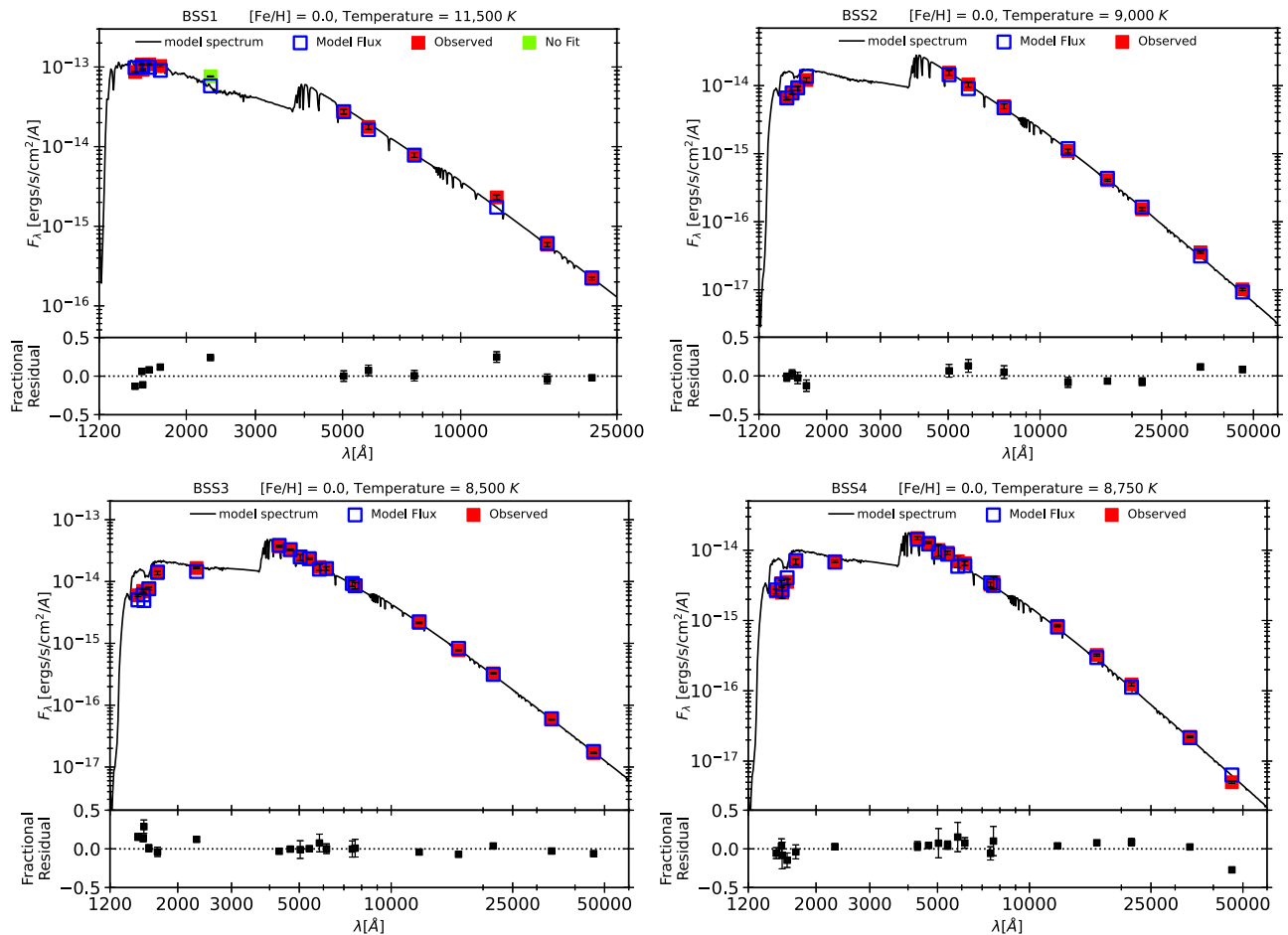


Figure 9. SEDs of four BSSs detected with UVIT. Extinction corrections have been incorporated in all the observed photometric fluxes from UV to IR. The BSS IDs adopted in this work are shown in each figure. The gray color presents the best-fitting Kurucz model spectrum in all the plots. Data points that are excluded in the SED fit are shown with orange color-filled symbols. The bottom panels in all the SEDs illustrate the residuals between the observed fluxes and model predictions.

Table 2
Stellar Parameters Obtained from Best-fit SEDs of BSSs Detected with UVIT in NGC 2818

Star ID	R.A. (deg)	Decl. (deg)	T_{eff} (K)	$\frac{L}{L_{\odot}}$	$\frac{R}{R_{\odot}}$	χ^2_{red}	Vgf	Vgf _b	$\frac{N_{\text{fit}}}{N_{\text{tot}}}$
BSS1	139.0306	-36.59184	11,500 ± 250	91.55 ± 17.54	2.39 ± 0.22	12.9	12.9	1.53	11/12
BSS2	139.0279	-36.59178	9000 ± 250	32.99 ± 6.31	2.31 ± 0.21	3.1	3.1	0.88	12/12
BSS3	139.1633	-36.43083	8500 ⁺⁵⁰⁰ ₋₂₅₀	52.28 ± 9.84	3.30 ± 0.31	4.8	4.8	1	19/19
BSS4	139.0276	-36.6423	8750 ± 250	20.97 ± 3.94	1.94 ± 0.18	4.9	4.9	0.91	19/19

Note. Column 1 lists the star IDs used in the paper. Columns 2 and 3 display the R.A. and decl. of all the stars considered for fitting, respectively. The T_{eff} , luminosities, and radii of all stars, along with their errors, are tabulated in columns 4, 5, and 6, respectively. Columns 7 and 8 lists the reduced- χ^2 values corresponding to the best fit and ratio of the number of photometric data points ($\frac{N_{\text{fit}}}{N_{\text{tot}}}$) used for the fit to the total number of available data points.

model spectrum created using the parameters corresponding to the best-fit SED. The star IDs adopted in this work are displayed at the top of each SED. We observe that the SEDs of all BSSs are seemed to be well-fitted with a single model, as the residuals are close to zero in all SEDs. Since the observed flux errors are very small for all the filters used, the error bars (shown with black color) are smaller than the data points. We list their parameters corresponding to the best fit in Table 2. We obtain Vgf_b values for all BSSs to be around 1, indicating good SED fits, and all the derived fundamental parameters are also reliable. The BSSs have a T_{eff} range of 8500–11,500 K and radii of 1.9–3.3 R_{\odot} . Now, here arises the two possibilities about the nature of these

stars: (1) either all the BSSs are single stars (2) or they are binaries with a very faint companion, not able to be detected by the UVIT observations. If these stars are single, they are likely to be formed via the merger of the component stars in a binary.

5.2. YSSs

Figure 10 presents the SEDs of the two stars classified as YSSs in this work. In this figure, the lower panel represents the fractional residuals, i.e., the ratio of the difference between the observed and model flux ($F_{\text{obs}} - F_{\text{model}}$) and the observed flux at every given data point. We can see in Figure 10 that both YSSs are showing significant UV excess as a single model

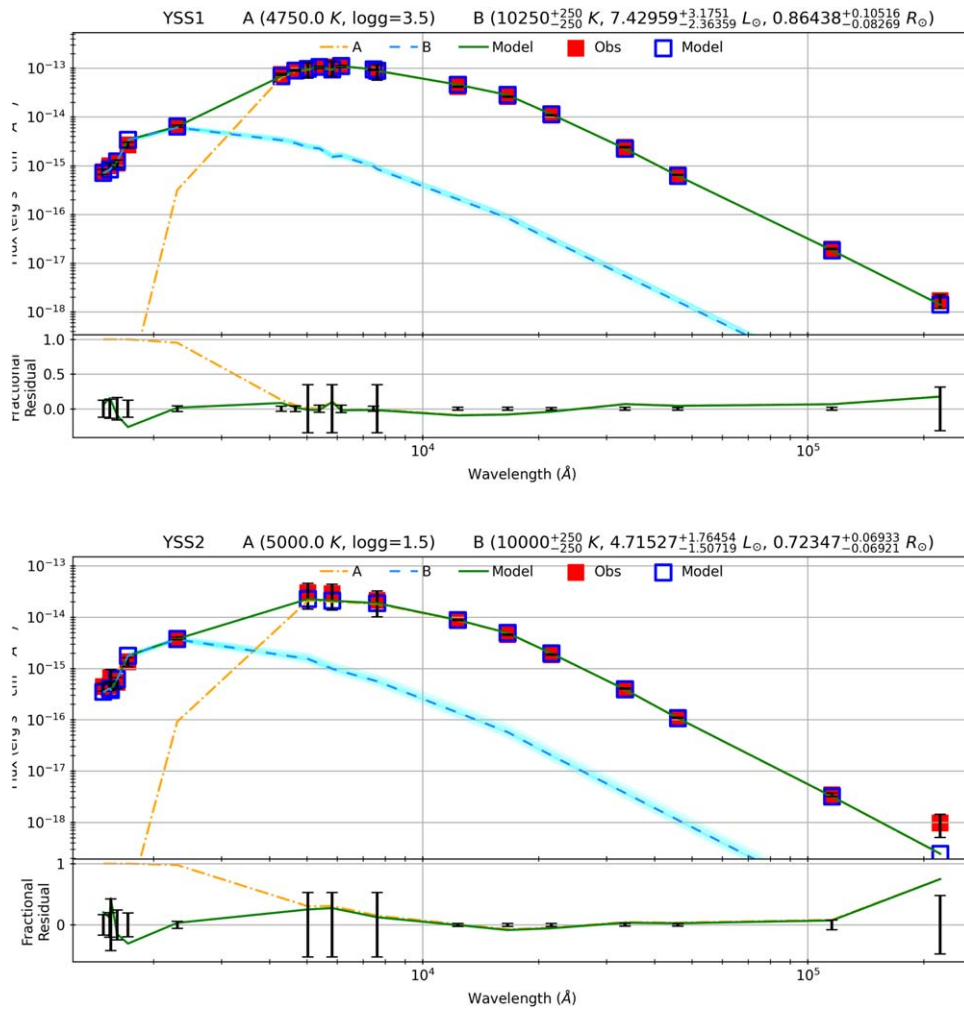


Figure 10. Double-fit SEDs of the YSSs. The meanings of all the symbols are displayed in the legend. The star IDs and parameters of the two components obtained from the fits are shown at the top of both SED plots. The green color represents the composite model flux along with the observed fluxes marked with red symbols. The orange dashed–dotted and blue dashed lines indicate the Kurucz and Koester models used to fit the star’s cooler and hotter components, respectively. The middle panel presents the fractional residuals (orange dashed line) corresponding to the single fit as well as the composite fit (green solid line). The fractional observational uncertainties in the flux are also shown here. The values of χ^2_{red} and modified χ^2_{red} parameter, namely vgf_b^2 , representing the best fit are displayed in the lower panel.

could not fit the entire SED. It can also be noticed that the fractional residual plots show a rise in flux at UV wavelengths for the single spectrum fits (shown as the orange dashed–dotted line in the figure). To fit the hotter component of the system, first, we gave excess for wavelength less than 3000 Å and fitted the cooler component that includes the optical and IR data points with the Kurucz model by selecting a T_{eff} range from 3500 to 50,000 K and $\log g$ from 1.5 to 2.5 dex. From the single fit, the computed values of T_{eff} of YSS1 and YSS2 are 4750 K and 5000 K, respectively. The radii of YSS1 and YSS2 are $27 R_{\odot}$ and $\sim 11 R_{\odot}$, respectively. From their temperatures and radii, we infer that they are in the giant phase of stellar evolution. After obtaining the stellar parameters of the cooler component, then we used a binary SED-fitting⁶ code to fit the hotter part of the SED. The full details of this code are well described by Jadhav et al. (2021). As we expect the hotter component to be compact, we have used a Koester WD model (Tremblay & Bergeron 2009; Koester 2010). In this model, the ranges of free parameters T_{eff} and $\log g$ are 5000–80,000 K and 6.5–9.5, respectively. The double fits of both stars are shown in Figure 10, where the Kurucz model fits are shown with

orange dashed–dotted lines, and the Koester model fits with light-blue dashed lines. The composite fits are marked with solid green lines. The fractional residuals in both plots are close to zero for all observed data points indicating how well the double-component fits reproduce the observed SEDs. This is even evident from the vgf_b values (close to 1) computed from the SED fitting of both stars. The estimated parameters of both YSSs from the best binary fit are tabulated in Table 3. From the double fit, we estimate the values of the T_{eff} of the hotter companion of YSS1 and YSS2 to be 10,250 K and 10,000 K, respectively. The values of parameters such as the T_{eff} , luminosities, and radii of the stars are mentioned at the top of each SED plot.

5.3. PN NGC 2818

As we have shown in the previous section, PN NGC 2818 most likely has a physical association with the cluster; it will be interesting to characterize its central star to obtain information about its progenitor. We can clearly see the CSPN in the FUV image, as shown in Figure 1, implying its very high temperature. The magnitude of the CSPN is a vital parameter to study its evolution as it can be used to determine its stellar parameters. The

⁶ https://github.com/jikrant3/Binary_SED_Fitting

Table 3
Derived Parameters of the YSS and MS Stars from the Composite SED Fits

Star ID	R.A. (deg)	Decl. (deg)	Type	Model Used	T_{eff} (K)	$\frac{L}{L_{\odot}}$	$\frac{R}{R_{\odot}}$	χ^2_{red}	Vgf	Vgf _b	$\frac{N_{\text{fit}}}{N_{\text{tot}}}$
YSS1	139.0523	−36.57946	A	Kurucz	4750 ± 125	338.1 ± 63.25	27.01 ± 2.49	5.6	5.6	0.36	20/20
			B	Koester	10,250 ± 250	7.43 ^{+3.17} _{−2.36}	0.864 ^{+0.105} _{−0.083}	4.3	4.3	0.61	
YSS2	138.9976	−36.58243	A	Kurucz	5000 ± 250	78.91 ± 15.55	10.93 ± 1	3.5	3.5	0.71	16/16
			B	Koester	10,000 ± 250	4.72 ^{+1.76} _{−1.51}	0.723 ^{+0.069} _{−0.069}	2.4	2.4	0.81	
MS	139.0592	−36.60989	A	Kurucz	6000 ± 125	18.35 ± 3.47	3.98 ± 0.37	7.3	7.2	0.99	18/18
			B	Kurucz	9000 ± 125	10.79 ± 2.04	1.36 ± 0.125	7.3	7.2	0.99	

Note. The different models used to fit the cooler (A) and hotter (B) components of the SEDs are presented in column 5. The rest of the columns have the same meaning as depicted in Table 2.

Table 4
Derived Parameters of PN NGC 2818 from the Best-fit SED

Star ID	R.A. (deg)	Decl. (deg)	Model Used	T_{eff} (K)	$\frac{L}{L_{\odot}}$	$\frac{R}{R_{\odot}}$	χ^2_{red}	Vgf	Vgf _b	$\frac{N_{\text{fit}}}{N_{\text{tot}}}$
PN NGC 2818	139.0061	−36.62707	TMAP(Grid3)	190,000 ± 8080.40	826.75 ± 225.21	0.026 ± 0.002	8.3	8.3	4.5	6/6

Note. The notation of all columns is the same as described in Table 2.

magnitude of the CSPN in optical filters was measured by Gathier & Pottasch (1988). As the CSPN is well observed in all FUV images, therefore we have calculated the magnitude of the central star by performing PSF photometry on the FUV images acquired in the 1st and 2nd epoch observations. We have subtracted the nebular background to assess the magnitude of the CSPN. The external extinction and distance to the nebula are considered to be the same as that of the cluster. Four FUV UVIT data points are combined with two optical photometric data points from Gathier & Pottasch (1988) to construct the observed SED of the nebula. As the central star seems to be very hot, we have fitted its SED with the Tübingen NLTE Model Atmosphere Package (TMAP) (Grid3) model used for hot stars (Rauch & Deetjen 2003; Werner et al. 2003). This model grid spans a range of atmospheric parameters such as $50,000 \text{ K} \leq T_{\text{eff}} \leq 190,000 \text{ K}$, $5.0 \leq \log g \leq 9.0$, and $0 \leq X_{\text{H}} \leq 1$. It is important to note that we took into account external extinction while fitting its SED but did not incorporate internal extinction in the nebula. We have noticed that T_{eff} derived using the TMAP model fit to the observed SED corresponds to their upper limits, which indicates that this star is likely to be hotter than the estimated temperature from this model. The stellar parameters computed from the best-fit SED of the nebula are summarized in Table 4.

5.4. MS Stars

We also have constructed SEDs for the MS stars detected with UVIT, for which rotational velocity information was available in the literature to investigate their nature. Apart from that, we also have considered all MS stars for an SED analysis whose rotational velocities were not estimated earlier, and their positions in all FUV–optical CMDs were not matched with their expected ones. 31 MS stars with known rotational velocities are identified with UVIT in the two epochs. Other than these stars, six MS stars are brighter than the MSTO in the FUV CMDs. We have used Kurucz models to fit their observed SEDs to obtain their physical parameters and check for the

existence of binarity. Out of the 37 stars, we observed that only one MS star shows significant FUV excess, as displayed in the right panel of Figure 11, whereas the other stars show less or mild UV excess that could not be fitted with a double-component SED. Chromospheric activity in the above star cannot account for its UV excess as it is exceptionally high compared to the model. The other possibility to explain this excess is the presence of a hot companion that mainly emits at shorter wavelengths. To account for the presence of a hot companion, we fitted the entire SED with the Kurucz model using the binary fit task from VOSA. The double-component fit for this star is found to be satisfactory (right panel of Figure 11), and the best-fit parameters computed are tabulated in Table 3. The radii of both components suggest that they are not quite on the MS. The cooler companion is likely to be a subgiant ($R/R_{\odot} \sim 4.0$), whereas the hot companion has a smaller radius ($R/R_{\odot} \sim 1.36$) when compared to a MS star of similar temperature ($R/R_{\odot} \sim 6.0$). It might be possible that this is a post-mass-transfer system where the hotter component is the donor, and the cooler component is still bloated after gaining mass. The rotational velocity (V_{sini}) of this star is around 39 km s^{-1} .

6. Evolutionary Status

Placing stars on an H-R diagram provides information about their evolutionary stage and helps in probing the nature of the hot companions in the case of binary stars. To examine the evolutionary statuses of the exotic stars considered in this study, we have plotted theoretical evolutionary sequences starting from the MS to the moment the star has entered the tip-of-the-RGB stage. These tracks are taken from MIST models computed by Choi et al. (2016) and Paxton et al. (2018), and are selected for cluster age and metallicity close to that of the cluster. The stellar parameters estimated from the single-SED fits for the four BSSs are plotted in an H-R diagram. The meaning of the color and symbols are marked in Figure 12. We

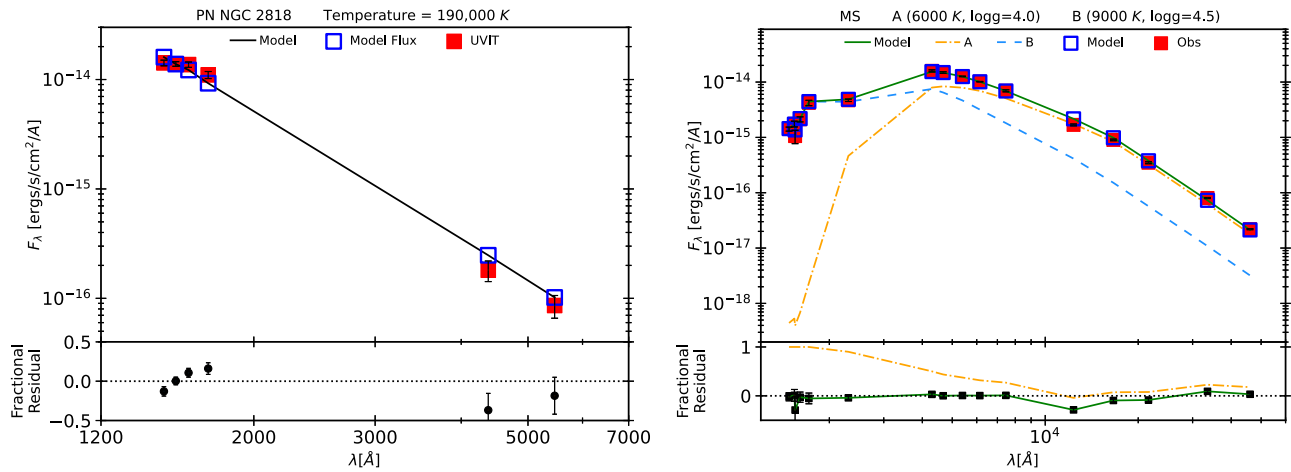


Figure 11. SED fit of the CSPN (left panel) and MS star (right panel) after taking into account extinction corrections. The black solid line represents the theoretical TMAP model fit to the observed fluxes shown with red symbols. The best-fit T_{eff} value is displayed in the figure. The rest of the details are the same as in Figures 9 and 10.

can notice in Figure 12 that the BSSs are lying bluer than the MS track, suggesting that these four stars belong to the BSS evolutionary phase.

The locations of the two YSSs on the H-R diagram are near the theoretical RGB sequence. This indicates that their progenitors (BSSs) have already evolved into a giant phase where the contracting helium core is surrounded by a hydrogen-burning shell. The hot companions of both YSSs seemed to be compact in nature, as indicated by their estimated radii, suggesting they might belong to the WD, extremely low mass (ELM) WD, or subdwarf stages of stellar evolution. In addition to the MS tracks, we have presented DA-type WD cooling sequences with masses of $0.5 M_{\odot}$ and $0.2 M_{\odot}$ taken from Tremblay et al. (2011) in Figure 12. From comparing the positions of the hot companions of both YSSs with the theoretical WD cooling tracks, we notice that their locations are not reproduced by them, implying that they still have not entered the WD stage. While there are non-DA-type WDs that are believed to result from mergers, they are not expected to be found in OCs because the merger process would take longer than the age of the cluster.

In order to find out where ELM WDs fall in the H-R diagram, we have used the field ELM WD catalog provided by Brown et al. (2016). They have estimated the T_{eff} and $\log g$ values of the ELM WD sample in their paper. To place them on the T_{eff} versus luminosity plane, SED-fitting technique is used to estimate the luminosity of all ELM WDs (Priv. Comm. Vikrant Jadhav). The extinction correction has been incorporated in all stars. All field ELM WDs are marked as cyan-filled symbols in Figure 12. We note that the hot companions of the YSSs are more luminous than the field ELMs with similar temperatures.

As the locations of the binary companions of YSSs are not reproduced by the WD tracks as well as ELM WDs, we further suspect that they might belong to a class of A-type subdwarfs (sdA) as they are lying near the general location of subdwarfs in the H-R diagram. sdA stars are supposed to occupy the location between dwarfs and WDs in the H-R diagram; hence, they are more compact than dwarfs, indicating a higher $\log g$ value. Brown et al. (2017) performed a detailed study of sdA stars to investigate their physical nature and a possible link to ELM WDs. We used their field sdA catalog to locate their

positions on the H-R diagram. As only the effective temperatures of all sdA stars are available in the catalog, we used the SED-fitting technique to determine their luminosities. The extinction in the visual band (A_V) for these stars was estimated using the reddening maps provided by Schlafly & Finkbeiner (2011). We have taken care of the extinction correction in the observed fluxes in the different bands of all the sdA stars considered here. The distances to these stars are available in the Gaia EDR3 catalog. We have used the distances reported by Bailer-Jones et al. (2021), estimated using the Gaia EDR3 catalog, and they all fall within the range of ~ 1.5 – 8 kpc. The sdA stars are displayed with purple-filled symbols in the H-R diagram. The hot companions of the YSSs are found to be hotter than the similarly luminous field sdAs and more luminous than the similarly hot field sdAs.

From this comparison, we suggest that they are most likely to be sdA stars formed through a binary mass-transfer scenario. These binaries are probably a post-mass-transfer system consisting of an A-type subdwarf candidate and a YSS. We also checked the positions of the hotter and cooler components of the MS star on the H-R diagram displayed with orange color symbols. The hotter component occupies a location bluer than theoretical isochrone, which might be evolving to an sdA-type star, whereas the cooler component occupies the location expected for subgiants. The evolution of this star might be similar to the YSS as the cooler component is evolving to the giant stage, whereas the hotter component later might end up as an sdA. Thus, we speculate that this system might be a progenitor of the YSSs detected in this cluster.

Further, we have used the post-AGB (pAGB) models computed by Miller Bertolami (2016) to deduce the evolutionary state of the CSPN. We adopted the cluster metallicity ($Z = \sim 0.02$ dex) to select the pAGB tracks. Tracks with a range of final masses as shown in Figure 12 are presented from the beginning of the pAGB phase when the H-rich envelope drops below $M_{\text{env}} = 0.01 M_{*}$ to the moment the star has already entered its WD cooling sequence at $L_{*} = L_{\text{Sun}}$. The estimated parameters of the PN from the SED fit are plotted in the H-R diagram (red filled symbols). From the comparison to these theoretical pAGB tracks, we observe that the CSPN is found to be located on the track (black dashed-dotted line)

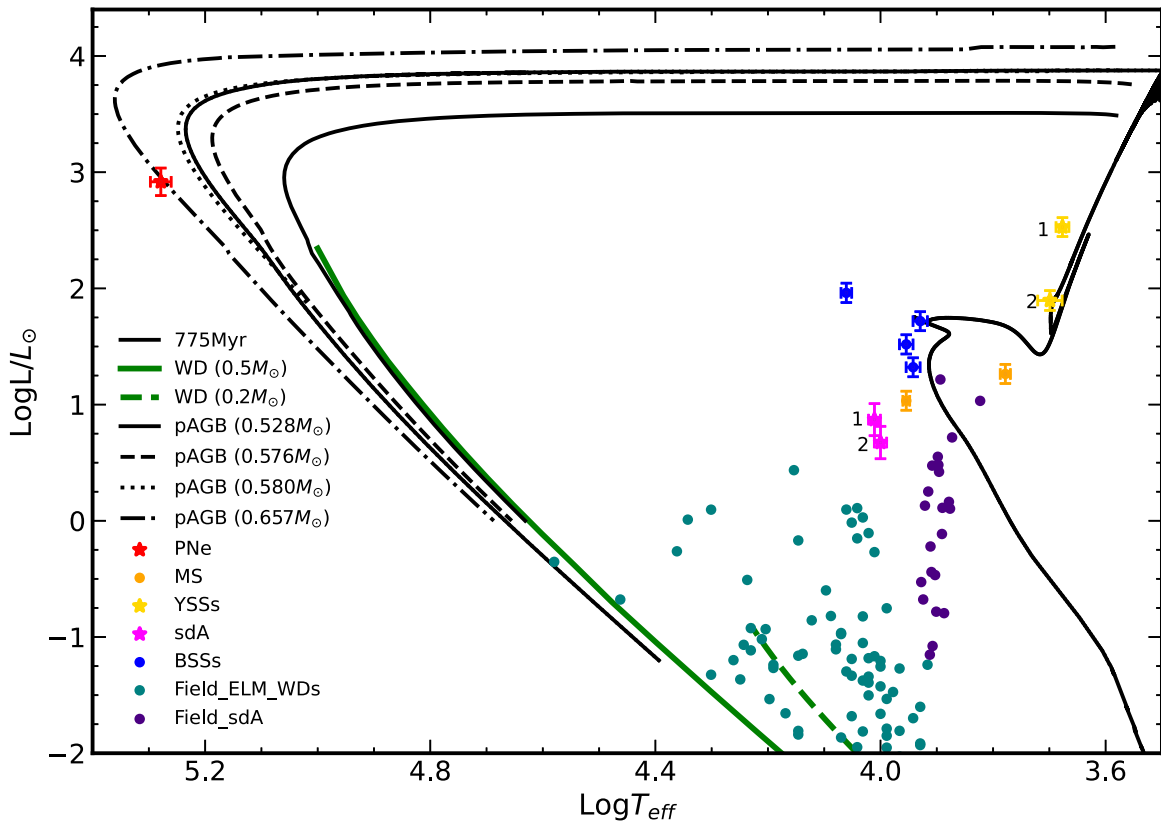


Figure 12. H-R diagram of the bright stars identified with UVIT. Various evolutionary tracks are presented from the beginning of the MS to the moment when a star has entered to the tip of the RGB stage, followed by the WD cooling sequences. All these tracks are generated for the cluster’s metallicity and age. pAGB sequences with different final masses are shown here to compare the location of the CSPN marked with a red star symbol. BSSs and YSSs are displayed with blue-filled circles and yellow star symbols, respectively. The hotter companions of the YSSs are shown with magenta star symbols. In addition, field ELM WDs and A-type subdwarfs represented with cyan and purple symbols, respectively, are also placed on the H-R diagram to compare the position of the hot companions of both YSSs. The green color solid and dashed lines correspond to the DA-WD tracks with different masses.

corresponding to the final mass $0.657 M_{\odot}$. It can be noted from here that the star has already entered the WD cooling phase.

7. Discussion

We have conducted an observational study of OC NGC 2818 and the PN within its field using FUV medium-resolution space-based imaging data from UVIT aboard AstroSat. This paper aims to use the most accurate and complete Gaia EDR3 data on stellar astrometry and photometry in the nearby intermediate-age OC NGC 2818 to establish the MPs of known stars and to deduce the evolutionary states of the exotic stars therein. Since the stars reside in the central area of the cluster, we have confined ourselves to consider only the inner part of the cluster with a radius of $30'$ and selected 37,508 stars brighter than $G = 21$ mag. Using the GMM method to pick out PM members, we have chosen 718 stars as cluster members with $P_{\mu} > 50\%$ and considered them further to identify their FUV counterparts with UVIT. FUV–optical and FUV CMDs were generated for the cluster members and overlaid with the MIST isochrones to compare the positions of the different observed evolutionary sequences with the theoretically expected ones. The MIST isochrones are found to match well with the observed sequences in the FUV–optical CMDs, but in the FUV CMDs, especially (F169M–F172M) versus G_{bp} , most of the detected stars in both filters are lying blueward of their expected locations from the isochrones.

In all FUV images, we have identified four BSSs, two YSSs, and the MS based on their locations in the optical as well as FUV–optical CMDs. Then, we performed an SED analysis to deduce their physical properties to evaluate their nature. The T_{eff} values of the BSSs estimated from the SED fits range from 8500 to 11,500 K, hinting that they are quite hot, consistent with the young age (700–800 Myr) of the cluster. In previous studies of BSSs in other OCs conducted using UVIT data, the T_{eff} range varies from cluster to cluster depending upon its age. The temperature range of BSSs in OC M67 (4 Gyr) is 6250–9000 K (Jadhav et al. 2019), in King 2 (6 Gyr) it is 5750–8500 K (Jadhav et al. 2021), and in OC NGC 188 (7 Gyr) it is 6100–6800 K (Gosnell et al. 2015). In intermediate-age OCs such as NGC 7789 (1.6 Gyr) (Vaidya et al. 2022) and NGC 2506 (2.2 Gyr) (Panthi et al. 2022), BSSs span a temperature range from 7250 to 10,250 K, and 7750–9750 K, respectively. The SEDs of all BSSs are well-fitted with a single model, and we suggest that collisions leading to mergers might explain their formation in this cluster. Another plausible possibility is that they might have a faint WD companion undetectable with UVIT. If this is the case, then the second prominent scenario to explain their existence in star clusters, i.e., mass transfer in close binaries, will dominate over the previous one. Moreover, mass transfer in binaries will dominate in OCs as they are less dense and compact than GC systems. Further, spectroscopic analysis of these stars will help to confirm their nature.

Two YSSs, from their SED fits, are found to be binaries, and the location of the YSSs and their hot components in the H-R diagram suggests that the cool components are already in the RGB phase. In contrast, the hot components most plausibly belong to the sdA class. We infer from here that these two stars are post-mass-transfer systems where the BSS (accretor) has evolved into the giant stage and became a YSS, and the donor star into an sdA. In addition, the spectroscopic study performed by Mermilliod et al. (2001) of RGB stars, including these two stars, found that they are spectroscopic binaries, confirming our result. The RVs estimated by them also verify their membership. Hence, we suggest that these two stars formed via a mass-transfer scenario in the cluster.

From a comparison of the distance, extinction, RV, and PM values of the PN with the cluster, it turns out that it is a most likely member of the cluster. Bohigas (2003, 2008) estimated T_{eff} from the ionization modeling of the nebula as $T_{\text{eff}} = 149,000$ K and a $\log g$ of 7.1 (however, this might also be dependent on the distance assumed). Mata et al. (2016) gives T_{eff} as 160,000 K. Gathier & Pottasch (1988) estimate an H I Zanstra temperature of 175,000 K and an He II Zanstra temperature of 215,000 K. Kohoutek et al. (1986) derived the luminosity ($L_* = 851 L_{\odot}$) and radius ($R_* = 0.038 R_{\odot}$) of the CSPN using optical observations, adopting an identical distance to the nebula as that of the cluster ($d = 3.5$ kpc). The atmospheric parameters of the CSPN determined using the SED-fitting technique are more or less in agreement with the previous estimations. Based on a comparison of the central star's location with the predicted ones from the theoretical models in the H-R diagram, the central star's mass turns out to be $0.66 M_{\odot}$. Cummings et al. (2018) presented the WD initial-final mass relation (IFMR) for progenitor stars of M_{initial} from 0.85 to $7.5 M_{\odot}$. In their Figure 5, they displayed a comparison of the IFMR estimated for the observed sample with theoretical isochrones. For a WD with a mass of $0.66 M_{\odot}$, the initial mass of the progenitor is estimated to be $\sim 2.1 M_{\odot}$ (from their Figure 5). In this work, the MSTO mass of this cluster determined using isochrone fit is $\sim 2 M_{\odot}$. The previously reported TO mass for this cluster and the initial mass of the nebula's progenitor are $\sim 2.1 M_{\odot}$, and $2.2 \pm 0.3 M_{\odot}$, respectively (Dufour 1984). Our estimations are consistent with the previous ones. From the comparison of the cluster's TO mass and progenitor mass, we infer that the PN is quite likely a cluster member. Thus, this study showcases the significance of using FUV data to study the exotic populations and late stages of the evolution of intermediate-mass stars in OCs.

8. Summary and Conclusions

The main results from this work can be summarized as follows:

1. In this study, we employed UVIT observations on board AstroSat to identify BSSs and YSSs in the OC NGC 2818, and also characterize the CSPN. We further created optical and UV-optical CMDs of member stars co-detected using UVIT and Gaia EDR3 data in this cluster.
2. The PM members of the cluster are obtained using Gaia EDR3 data, and we found that PN NGC 2818 might be a member of this cluster, consistent with previous studies.
3. As this cluster is young, hot and bright stars such as BSSs, YSSs, and MS are detected in all FUV images.
4. To compare the observations with theoretical predictions, optical and UV-optical CMDs are overlaid with


nonrotating MIST isochrones generated for the respective UVIT and Gaia filters. The theoretical isochrones reproduce the features of all CMDs quite well.

5. The FUV-optical CMDs prominently show the eMSTO phenomenon already reported in this cluster, consistent with previous studies.
6. We characterized the four detected BSSs in the cluster, and a single model fits well to all the observed SEDs. We suggest from the single model fits that these stars might have a faint WD companion that could not be detected with UVIT's detection limit or result from the merger of two close binaries.
7. We suggest the presence of two YSSs in this cluster based on their locations in the CMDs. Both YSSs were found to have excess flux in the UV, connected to binarity. They are confirmed spectroscopic binaries, and their hot companions are compact objects, likely sdA stars. Based on these results, we conclude that they are the products of binary mass transfer.
8. From comparing the position of the CSPN with theoretical pAGB evolutionary tracks, we found that it has entered the WD cooling phase, and its mass is found to be $\sim 0.66 M_{\odot}$. The mass of the progenitor corresponding to a WD of mass $0.66 M_{\odot}$ would be $\sim 2.1 M_{\odot}$, similar to the TO mass of the cluster, further confirming its membership.

We thank the anonymous referee for their valuable comments and suggestions. A.S. acknowledges support from SERB Power Fellowship. S.R. would like to thank Vikrant Jadhav for providing us with the field ELM WDs SED fit parameters. S.R. thanks Sonith L. S. for the fruitful discussions. This publication utilizes the data from AstroSat mission's UVIT, which is archived at the Indian Space Science Data Centre (ISSDC). The UVIT project is a result of collaboration between IIA, Bengaluru, IUCAA, Pune, TIFR, Mumbai, several centers of ISRO, and CSA. This research made use of VOSA, developed under the Spanish Virtual Observatory project supported by the Spanish MINECO through grant AyA2017-84089. This research also made use of the Aladin sky atlas developed at CDS, Strasbourg Observatory, France (Bonnarel et al. 2000).

Software: GaiaTools (Vasiliev 2019), Topcat (Taylor 2011), Matplotlib (Hunter 2007), NumPy (van der Walt et al. 2011), Scipy (Oliphant 2007; Millman & Aivazis 2011), Astropy (Astropy Collaboration et al. 2013, 2018) and Pandas (McKinney 2010).

ORCID iDs

Sharmila Rani  <https://orcid.org/0000-0003-4233-3180>
 Gajendra Pandey  <https://orcid.org/0000-0001-5812-1516>
 Annapurni Subramaniam  <https://orcid.org/0000-0003-4612-620X>
 N. Kameswara Rao  <https://orcid.org/0000-0002-8414-8541>

References

- Ahumada, J. A., & Lapasset, E. 2007, *A&A*, 463, 789
 Alam, S., Albareti, F. D., Allende Prieto, C., et al. 2015, *ApJS*, 219, 12
 Astropy Collaboration, Price-Whelan, A. M., Sipőcz, B. M., et al. 2018, *AJ*, 156, 123
 Astropy Collaboration, Robitaille, T. P., Tollerud, E. J., et al. 2013, *A&A*, 558, A33

- Bailer-Jones, C. A. L., Rybizki, J., Fouesneau, M., Demleitner, M., & Andrae, R. 2021, *AJ*, **161**, 147
- Bastian, N., & de Mink, S. E. 2009, *MNRAS Lett.*, **398**, L11
- Bastian, N., Kamann, S., Cabrera-Ziri, I., et al. 2018, *MNRAS*, **480**, 3739
- Bayo, A., Rodrigo, C., Barrado Y Navascués, D., et al. 2008, *A&A*, **492**, 277
- Bianchi, L., Shiao, B., & Thilker, D. 2017, *ApJS*, **230**, 24
- Boffin, H. M. J., Carraro, G., & Beccari, G. 2015, *Ecology of Blue Straggler Stars*, Astrophysics and Space Science Library, Vol. 413 (Berlin: Springer)
- Bohigas, J. 2003, *RMxAA*, **39**, 149
- Bohigas, J. 2008, *ApJ*, **674**, 954
- Bonnarel, F., Fernique, P., Bienaymé, O., et al. 2000, *A&AS*, **143**, 33
- Brandt, T. D., & Huang, C. X. 2015, *ApJ*, **807**, 24
- Brown, W. R., Gianninas, A., Kilic, M., Kenyon, S. J., & Allende Prieto, C. 2016, *ApJ*, **818**, 155
- Brown, W. R., Kilic, M., & Gianninas, A. 2017, *ApJ*, **839**, 23
- Cabrera-Ziri, I., Bastian, N., Hilker, M., et al. 2016, *MNRAS*, **457**, 809
- Cantat-Gaudin, T., & Anders, F. 2020, *A&A*, **633**, A99
- Cantat-Gaudin, T., Anders, F., Castro-Ginard, A., et al. 2020, *A&A*, **640**, A1
- Castelli, F., Gratton, R. G., & Kurucz, R. L. 1997, *A&A*, **318**, 841
- Castelli, F., & Kurucz, R. L. 2003, in *IAU Symp. 210, Modelling of Stellar Atmospheres*, ed. N. Piskunov, W. W. Weiss, & D. F. Gray (Cambridge: Cambridge Univ. Press), **A20**
- Choi, J., Dotter, A., Conroy, C., et al. 2016, *ApJ*, **823**, 102
- Cummings, J. D., Kalirai, J. S., Tremblay, P. E., Ramirez-Ruiz, E., & Choi, J. 2018, *ApJ*, **866**, 21
- Cutri, R. M., Skrutskie, M. F., van Dyk, S., et al. 2003, *2MASS All Sky Catalog of point sources* (Pasadena, CA: IRSA)
- Cutri, R. M., Wright, E. L., Conrow, T., et al. 2021, *yCat*, **2328**, 0
- de Marchi, F., de Angeli, F., Piotto, G., Carraro, G., & Davies, M. B. 2006, *A&A*, **459**, 489
- Dufour, R. J. 1984, *ApJ*, **287**, 341
- Ferraro, F. R., Lanzoni, B., Dalessandro, E., et al. 2012, *Natur*, **492**, 393
- Fitzpatrick, E. L. 1999, *PASP*, **111**, 63
- Frew, D. J., Parker, Q. A., & Bojičić, I. S. 2016, *MNRAS*, **455**, 1459
- Gaia Collaboration, Helmi, A., van Leeuwen, F., et al. 2018, *A&A*, **616**, A12
- Gathier, R., & Pottasch, S. R. 1988, *A&A*, **197**, 266
- Gosnell, N. M., Mathieu, R. D., Geller, A. M., et al. 2015, *ApJ*, **814**, 163
- Gossage, S., Conroy, C., Dotter, A., et al. 2019, *ApJ*, **887**, 199
- Henden, A. A., Levine, S., Terrell, D., & Welch, D. L. 2015, *AAS Meeting Abstracts*, **225**, 336.16
- Hills, J. G., & Day, C. A. 1976, *ApL*, **17**, 87
- Hunter, J. D. 2007, *CSE*, **9**, 90
- Iben, I. J., & Tutukov, A. V. 1999, in *ASP Conf. Ser. 169, 11th European Workshop on White Dwarfs*, ed. S. E. Solheim & E. G. Meistas (San Francisco, CA: ASP), **432**
- Indebetouw, R., Mathis, J. S., Babler, B. L., et al. 2005, *ApJ*, **619**, 931
- Jadhav, V. V., Pandey, S., Subramaniam, A., & Sagar, R. 2021, *JApA*, **42**, 89
- Jadhav, V. V., Sindhu, N., & Subramaniam, A. 2019, *ApJ*, **886**, 13
- Jadhav, V. V., & Subramaniam, A. 2021, *MNRAS*, **507**, 1699
- Jordan, C., & Linsky, J. L. 1987, *Exploring the Universe with the IUE Satellite*, Astrophysics and Space Science Library ed. Y. Kondo & W. Wamsteker, Vol. 129 (Dordrecht: Reidel), **259**
- Kharchenko, N. V., Piskunov, A. E., Schilbach, E., Röser, S., & Scholz, R. D. 2013, *A&A*, **558**, A53
- Knigge, C., Dieball, A., Maíz Apellániz, J., et al. 2008, *ApJ*, **683**, 1006
- Koester, D. 2010, *MmSAI*, **81**, 921
- Kohoutek, L., Roth-Hoepfner, M. L., & Laustsen, S. 1986, *A&A*, **162**, 232
- Kwitter, K. B., Méndez, R. H., Peña, M., et al. 2014, *RMxAA*, **50**, 203
- Landsman, W., Aparicio, J., Bergeron, P., Di Stefano, R., & Stecher, T. P. 1997, *ApJL*, **481**, L93
- Lindgren, L., Hernández, J., Bombrun, A., et al. 2018, *A&A*, **616**, A2
- Linsky, J. L., & Haisch, B. M. 1979, *ApJ*, **229**, L27
- Linsky, J. L., Wood, B. E., Youngblood, A., et al. 2020, *ApJ*, **902**, 3
- Mata, H., Ramos-Larios, G., Guerrero, M. A., et al. 2016, *MNRAS*, **459**, 841
- McCrea, W. H. 1964, *MNRAS*, **128**, 147
- McKinney, W. 2010, in *Proc. 9th Python in Science Conf.*, ed. S. van der Walt & J. Millman (Austin, TX: SciPy), 51
- Meatheringham, S. J., Wood, P. R., & Faulkner, D. J. 1988, *ApJ*, **334**, 862
- Mermilliod, J. C., Clariá, J. J., Andersen, J., Piatti, A. E., & Mayor, M. 2001, *A&A*, **375**, 30
- Miller Bertolami, M. M. 2016, *A&A*, **588**, A25
- Millman, K., & Aivazis, M. 2011, *CSE*, **13**, 9
- Milne, D. K., & Aller, L. H. 1975, *A&A*, **38**, 183
- Niederhofer, F., Georgy, C., Bastian, N., & Ekström, S. 2015, *MNRAS*, **453**, 2070
- Oliphant, T. E. 2007, *CSE*, **9**, 10
- Pallavicini, R., Golub, L., Rosner, R., et al. 1981, *ApJ*, **248**, 279
- Panthi, A., Vaidya, K., Jadhav, V., et al. 2022, *MNRAS*, **516**, 5318
- Paxton, B., Schwab, J., Bauer, E. B., et al. 2018, *ApJS*, **234**, 34
- Pederos, M. 1989, *AJ*, **98**, 2146
- Perets, H. B., & Fabrycky, D. C. 2009, *ApJ*, **697**, 1048
- Postma, J. E., & Leahy, D. 2017, *PASP*, **129**, 115002
- Pottasch, S. R. 1984, *Planetary Nebulae. A Study of Late Stages of Stellar Evolution* ed. S. R. Pottasch, Vol. 107 (Dordrecht: Springer)
- Rain, M. J., Ahumada, J. A., & Carraro, G. 2021, *A&A*, **650**, A67
- Rani, S., Pandey, G., Subramaniam, A., et al. 2021, *ApJ*, **923**, 162
- Rauch, T., & Deetjen, J. L. 2003, *ASP Conf. Ser. 288, Stellar Atmosphere Modeling* ed. I. Hubeny, D. Mihalas, & K. Werner (San Francisco, CA: ASP), **103**
- Rebassa-Mansergas, A., Solano, E., Jiménez-Esteban, F. M., et al. 2021, *MNRAS*, **506**, 5201
- Riello, M., De Angeli, F., Evans, D. W., et al. 2021, *A&A*, **649**, A3
- Santana, F. A., Muñoz, R. R., Geha, M., et al. 2012, in *ASP Conf. Ser. 458, Galactic Archaeology: Near-Field Cosmology and the Formation of the Milky Way*, ed. W. Aoki et al. (San Francisco, CA: ASP), **339**
- Santucci, R. M., Placco, V. M., Rossi, S., et al. 2015, *ApJ*, **801**, 116
- Schlafly, E. F., & Finkbeiner, D. P. 2011, *ApJ*, **737**, 103
- Sindhu, N., Subramaniam, A., & Radha, C. A. 2018, *MNRAS*, **481**, 226
- Stetson, P. B. 1987, *PASP*, **99**, 191
- Sun, W., de Grijs, R., Deng, L., & Albrow, M. D. 2021, *MNRAS*, **502**, 4350
- Surendiranath, R., Kameswara Rao, N., Sagar, R., Nathan, J. S., & Ghosh, K. K. 1990, *JApA*, **11**, 151
- Tandon, S. N., Hutchings, J. B., Ghosh, S. K., et al. 2017, *JApA*, **38**, 28
- Tandon, S. N., Postma, J., Joseph, P., et al. 2020, *AJ*, **159**, 158
- Taylor, M. 2011, *TOPCAT: Tool for OPERations on Catalogues And Tables*, Astrophysics Source Code Library, ascl:1101.010
- Tifft, W. G., Connolly, L. P., & Webb, D. F. 1972, *MNRAS*, **158**, 47
- Tremblay, P. E., & Bergeron, P. 2009, *ApJ*, **696**, 1755
- Tremblay, P. E., Bergeron, P., & Gianninas, A. 2011, *ApJ*, **730**, 128
- Vaidya, K., Panthi, A., Agarwal, M., et al. 2022, *MNRAS*, **511**, 2274
- van der Walt, S., Colbert, S. C., & Varoquaux, G. 2011, *CSE*, **13**, 22
- Vasiliev, E. 2019, *MNRAS*, **484**, 2832
- Vázquez, R. 2012, *ApJ*, **751**, 116
- Weidemann, V. 2000, *A&A*, **363**, 647
- Werner, K., Deetjen, J. L., Dreizler, S., et al. 2003, in *ASP Conf. Ser. 288, Stellar Atmosphere Modeling*, ed. I. Hubeny, D. Mihalas, & K. Werner (San Francisco, CA: ASP), **31**
- Whitford, A. E. 1958, *AJ*, **63**, 201
- Zhang, C. Y. 1995, *ApJS*, **98**, 659